ILASS-Americas 31st Annual Conference on Liquid Atomization and Spray Systems, May 2021

Validation of Inflow Modeling for Numerical Simulations of Air-blast Atomization Against Experimental Backlit Imaging and Radiographs

Lam Vu*[1] ,* Nathanaël Machicoane[2,4], Danyu Li[3], Timothy Morgan[3], Theodore J. Heindel[3], Alberto Aliseda[2], Olivier Desjardins[1]

[1]Department of Mechanical and Aerospace Engineering,
Cornell University, Ithaca, NY, USA
[2]Department of Mechanical Engineering,
University of Washington, Seattle, WA, USA
[3]Department of Mechanical Engineering,
Iowa State University, Ames, IA, USA
[4]Univ. Grenoble Alpes, CNRS, Grenoble INP, LEGI, 38000 Grenoble, France

Abstract

Sprays appear in a variety of industrial applications ranging from powder production used in additive manufacturing to fuel nozzles. Air-blast atomization is a specific injection strategy whereby a high-speed gas shears and destabilizes a low-speed liquid which causes a cascade of instabilities leading to the creation of a spray. The flow physics around the nozzle are challenging to quantify and complex. Inside the nozzle, traditional PIV and hot-wire methods cannot be used to measure turbulence and boundary layer growth and at the nozzle exit, radiographs and back-lit images show complex time-varying wetting and contact line dynamics. In this study, we explore different strategies to model the inflow and compare them against equivalent path length data (EPL), a measure of the liquid depth along a line-of-sight. In particular, we discuss the impact of different contact line models and the importance of modeling the flow inside the nozzle.

*Corresponding Author: lxv2@cornell.edu

Introduction

Liquid sprays play a pivotal role in many engineering applications such as agricultural sprays, medical coatings, and liquid fuel combustion. Understanding the spray formation and dispersion process is crucial for design of fuel efficient and low pollutant emitting combustion systems.

Air-blast atomization is a specific spray strategy whereby a high-speed gas shears and destabilizes a low-speed liquid stream which results in a cascade of instabilities that form a spray. Many studies have been performed on air-blast atomization (e.g., [1, 2, 3, 4]) which have explained the effect of swirl and gas boundary layer thickness and provided correlations for liquid corrugation sizes, among other things. More recently, X-ray imaging utilizing specialized facilities at Argonne National Lab's Advanced Photon Source has been used successfully to visualize 3D liquid structures in the flow, enabling the study of physics like bubble entrainment and contact line dynamics [5, 6]. Despite extensive research, comparative studies between simulations and experiments remain limited [7, 8] and little literature exist on the computational inflow boundary conditions needed to obtain liquid dynamics seen under experimental conditions. Most studies have relied on analytical gas velocity profiles with a specified boundary layer thickness [4, 7] or connected velocity profiles between the liquid and gas [8, 9]. In both cases, modeling efforts related to the internal nozzle flow and the interaction between the interface and nozzle tip are reduced.

In this study, we discuss different inflow modeling strategies and their impact on liquid dynamics. Specifically, we explore the impact of the contact line model and the importance of modeling the flow inside the nozzle. We evaluate the effectiveness of the described models by comparing against experimental equivalent path length data (EPL), a measure of the liquid depth along a line-of-sight, and back-lit imaging.

Numerical Methods

We consider liquid-gas flows governed by the continuity equation

$$\frac{\partial \rho}{\partial t} + \nabla \cdot (\rho \mathbf{u}) = 0 \tag{1}$$

and the incompressible Navier-Stokes equation

$$\frac{\partial \rho \mathbf{u}}{\partial t} + \nabla \cdot (\rho \mathbf{u}\mathbf{u}) = -\nabla p + \nabla \cdot \left(\mu \left[\nabla \mathbf{u} + \nabla \mathbf{u}^{\mathsf{T}}\right]\right) + \rho \mathbf{g}, \tag{2}$$

where ρ is the fluid density, μ is the dynamic viscosity, $\mathbf{u}$ is the velocity, p is the pressure, $\mathbf{g}$ is the gravitational acceleration, and t is time. Fluid properties are constant within each phase but differ between the phases. We use subscripts l and g to denote liquid and gas quantities, respectively. If Γ indicates the interface and $\left[\ \right]_\Gamma$ indicates the jump of a property across the interface, then the jump in density and viscosity across the interface are $\left[\rho\right]_\Gamma = \rho_l - \rho_g$ and $\left[\mu\right]_\Gamma = \mu_l - \mu_g$, respectively. The velocity is continuous across the interface, hence $\left[\mathbf{u}\right]_\Gamma = 0$, and the pressure jump across the interface is given by

$$\left[p\right]_\Gamma = \sigma\kappa + 2\left[\mu\right]_\Gamma \mathbf{n}^{\mathsf{T}} \cdot \nabla \mathbf{u} \cdot \mathbf{n}, \tag{3}$$

where σ is the surface tension coefficient, κ is the interface curvature, and $\mathbf{n}$ is the interface normal. The equations are solved using an in-house, conservative, finite volume flow solver for low Mach number flows [10]. Phase tracking is handled with a geometric, semi-Lagrangian Volume-of-Fluid method [11]. This solver is second-order accurate in time and space and, away from the interface, is discretely kinetic energy conserving. Inside each computational cell, the interface is represented locally as a plane using piecewise linear interface reconstruction (PLIC) with the plane normal calculated using LVIRA [12]. To capture sub-grid scale effects, a dynamic Smagorinsky turbulence model [13] and at walls, a sub-grid scale contact line model are employed [14]. The curvature of the interface is calculated using parabolic surface fits. The pressure jump due to this curvature is then embedded as a source term in the pressure Poisson equation using a continuum surface force approach [15].

Experimental Methods

A canonical coaxial two-fluid atomizer is used for the experimental investigations. Air flows through 4 inlets perpendicular to the nozzle axis, and along converging cubic-spline shaped inner and outer walls to form a round annular turbulent jet, around a laminar circular water jet. The inner wall separating liquid and gas streams has an inner and outer dimension of d_l and D_l while the outer wall has an inner and outer dimension of d_g and D_g. x denotes the downstream direction while y and z are the perpendicular directions. The near-field of the atomizer is characterized using visible light at University of Washington and synchrotron X-rays at the Advanced Photon Source of Argonne National Laboratory. In the former, high spatial and temporal resolution back-lit imaging is considered, yielding almost binary images indicating liquid presence, where simple thresholding can be used to identify the liquid interface's time evolution [6]. In the latter, EPL is measured using a focused monochromatic X-ray

beam [5].

Simulation Set-up

To study the near-field region, we perform simulations of air-blast atomization in the same canonical nozzle using water and air properties. We consider one experimental condition at a gas Reynolds number, $Re_g \equiv 4Q/\sqrt{4\pi A_g}\nu_g$, of 21400, a liquid Reynolds number, $Re_l \equiv \rho_l U_l d_l/\mu_l$, of 1200, a momentum flux ratio, $M \equiv (\rho_g U_g^2)/(\rho_l U_l^2)$, of 6.4, and a Weber number, $We \equiv \rho_g(U_g - U_l)^2 d_l/\sigma$, of 39.1 where Q is the gas flow-rate, A_g is the gas flow-through area at the exit plane, ν_g is the gas kinematic viscosity and U_g and U_l are the gas and liquid bulk velocities, respectively. We present four simulations at this condition with various configurations. In all cases, the laminar liquid jet is prescribed with a plug flow and the gas jet is at a sufficiently high Reynolds number that a dynamic sub-grid scale turbulence model is needed and employed. To reduce computational cost, the atomization simulations in case 1 and 2 are performed without the nozzle, as shown in figure 1a, and the gas inflow prescribed is an analytical velocity profile that is a near uniform flow with a boundary layer thickness $\delta_g = 5.6H/\sqrt{Re_g}$ [3], where $H = (d_g - D_l)/2$ is the gas gap and $Re_g = \rho_g H U_g/\mu_g$. The inner wall separating the liquid and gas streams, the splitter plate, is modeled as a 0 velocity gas in case 1, implying the interface is pinned at d_l, and modeled as a 0 velocity liquid in case 2, implying the interface is pinned at D_l. In case 3, part of the nozzle is included in the simulation domain as seen in figure 1b and a uniform velocity profile matching Q is specified. A dynamic sub-grid scale (SGS) contact line model with a static contact line angle of 70° is employed which allows for a free moving contact line. In case 4, the same SGS dynamic contact line model is used and the internal flow of the nozzle is simulated and one-way coupled to the atomization simulation as illustrated in figure 1c. The simulations are performed on Cartesian meshes, with uniform mesh resolution of size $\Delta/d_l = 0.1$ for the atomization simulations and $\Delta/d_g = 0.1$ for the nozzle simulation in case 4. The converging nozzle walls are created by stair-stepping full cells that are treated as solid boundaries. The cases are summarized in table 1.

The corresponding radial gas velocity profiles at the nozzle exit plane, averaged in time and in θ, are shown in figure 2. Without any liquid present, the experimental gas velocity profiles are measured a small distance downstream of the nozzle using hot-wires. Because of the mismatch between conditions and measurement location, the comparison of velocity between simulations and experiments is mostly qualitative. All exit plane velocity statistics have satisfactory agreement with the experimental measurements. The boundary layer thickness calculated from the correlation for case 1 and 2 result in a thickness smaller than the experiment, case 3 and case 4.

Results and Discussion

Simulations are validated against experimental measurements of equivalent path length (EPL), a line-of-sight integration of liquid depth, obtained from focused monochromatic X-ray beam data. The EPL sampled along x, at the centerline ($y = 0$), gives a measure of the mean liquid depth as a function of the downstream distance and spatially quantifies how coherent the liquid is. Comparisons between simulations and experiments of this quantity are made in figure 3.

Case 1, where the splitter plate at the exit plane is modeled as a 0 velocity gas, is a seemingly straight-forward model since, without any flow, this region is the intersection between solid metal and static gas. This model implies that the interface pins at the inner edge of the splitter plate, d_l. As the liquid enters the domain, the combination of this pinning and the 0 velocity gas region forces the liquid to expand until the interface reaches the high-speed gas stream at $x \approx 0.25D_L$, as seen in figure 3 and it is only after this point that the liquid begins to destabilize. This phenomenon results in a near-nozzle behavior that is not consistent with experimental measurements. In the experimental X-ray imaging, it is observed that the interface dynamically wets the splitter plate and in some instances, can even wick up along the liquid outer wall at D_l. In case 2, the splitter plate is modeled as a 0 velocity liquid; this pins the interface to the outer edge of the splitter plate, D_l, and brings the interface closer to the high-speed gas stream which more closely matches the experimental conditions. The resulting centerline EPL from this case now decreases monotonically as is observed in the experiments. Although the pinned interface is a simple model, it fails to capture the dynamic motion of the contact line seen in experiments. Furthermore, the discrepancies in EPL profiles between case 1 and 2 highlight the strong dependence that the liquid destabilization has to interface pinning location, resulting in a model that is undesirably sensitive. A sub-grid scale contact line model allows the contact line to move freely along walls but requires a portion of the nozzle tip to be considered. Case 3 uses this sub-grid scale contact line model and includes a portion of the nozzle in the

simulation. These two factors result in a liquid that destabilizes at a rate that more closely matches the experiment. Case 4, which uses the same SGS contact line model but simulates the entire nozzle, results in an EPL profile similar to case 3 but differs in its flapping motion. Experimental back-lit imaging shows liquid flapping motion to be fairly axisymmetric. Table 2 shows time averaged plots of binarized liquid presence data for two orthogonal views. The figures in the table suggest that the flapping motion of the liquid jet is not axisymmetric in case 3 while it is in case 4. It is likely that, by including the full nozzle in case 4, a sufficient amount of disturbance to the flow is added from the turbulence inside the nozzle that it enables the liquid flapping instability to occur in all directions. However, in case 3, because such a short section of the nozzle is included in the domain, $2d_g$, most of the disturbances fed into this instability come from the pressure fluctuations downstream rather than the upstream flow inside the nozzle, resulting in the jet to predominately flap in the initial flapping direction selected by amplification of the numerical errors.

Conclusion

In this study, we have explored the effects of different inflow boundary conditions. We have shown that the pinning location of the interface has a significant impact on the destabilization of the liquid. Pinning to the inner diameter of the liquid leads to a increase in the EPL while pinning to the outer diameter leads to a monotonically decreasing EPL profile. We have shown that having a SGS dynamic contact line model which allows for a free moving contact line results in better experimental agreement. We have shown that with this contact line model, partially including the nozzle leads to liquid flapping in a preferred direction while including the entire nozzle leads to somewhat experimentally observed axisymmetric flapping. By establishing the near field region, we can move on to modeling of the mid-field region where thin-sheets form and burst and subsequent created droplets are dispersed. As these simulations are computationally demanding, mesh convergence studies are ongoing work.

Acknowledgements

This work was sponsored by the Office of Naval Research (ONR) as part of the Multidisciplinary University Research Initiatives (MURI) Program, under grant number N00014-16-1-2617. The views and conclusions contained herein are those of the authors only and should not be interpreted as representing those of ONR, the U.S. Navy or the U.S. Government.

A portion of this work was performed at the 7-BM beamline of the Advanced Photon Source, a U.S. Department of Energy (DOE) Office of Science User Facility operated for the DOE Office of Science by Argonne National Laboratory under Contract No. DE-AC02- 06CH11357.

Nomenclature

$\langle \cdot \rangle$	Time-averaging operator
Δ	Mesh spacing [m]
d_g	Gas inner diameter [m]
D_g	Gas inner diameter [m]
d_l	Liquid inner diameter [m]
D_l	Liquid inner diameter [m]
EPL	Equivalent path length [m]
κ	Curvature [m^{-1}]
$\mathbf{n}$	Interface normal vector
ρ_g	Gas density [kg m^{-3}]
ρ_l	Liquid density [kg m^{-3}]
σ	Surface tension coefficient [N m^{-1}]
t	Time [s]
μ_g	Gas dynamic viscosity [Pa s]
μ_l	Liquid dynamic viscosity [Pa s]
$\mathbf{u}$	Velocity vector [m s^{-1}]
U_l	Bulk gas velocity [m s^{-1}]
U_g	Bulk liquid velocity [m s^{-1}]
ν_g	Gas kinematic viscosity [$m^2 s^{-1}$]

References

[1] Hopfinger, E. and Lasheras, J., 2004, "Explosive breakup of a liquid jet by a swirling coaxial gas jet," Physics of Fluids, **8**, pp. 1696–1698.

[2] Lasheras, J., Villermaux, E., and Hopfinger, E., 1998, "Break-up and atomization of a round water jet by a high-speed annular air jet," Journal of Fluid Mechanics, **357**, pp. 351–379.

[3] Marmottant, P. H. and Villermaux, E., 2004, "On spray formation," Journal of Fluid Mechanics, **498**(498), pp. 73–111.

[4] Agbaglah, G., Chiodi, R., and Desjardins, O., 2017, "Numerical simulation of the initial destabilization of an air-blasted liquid layer," International Journal for Numerical Methods in Fluids, **812**, p. 1024.

[5] Bothell, J. K., Machicoane, N., Li, D., Morgan, T. B., Aliseda, A., Kastengren, A. L., and Heindel, T. J., 2020, "Comparison of X-ray and optical measurements in the near-field of an optically dense coaxial air-assisted atomizer," International Journal of Multiphase Flow, **125**, p. 103219.

[6] Machicoane, N., Ricard, G., Osuna-orozco, R., Huck, P. D., and Aliseda, A., 2020, "Influence of steady and oscillating swirl on the near-field spray characteristics in a two-fluid coaxial atomizer," International Journal of Multiphase Flow, **129**, p. 103318.

[7] Fuster, D., Bagué, A., Boeck, T., Le Moyne, L., Leboissetier, A., Popinet, S., Ray, P., Scardovelli, R., and Zaleski, S., 2009, "Simulation of primary atomization with an octree adaptive mesh refinement and VOF method," International Journal of Multiphase Flow, **35**, pp. 550–565.

[8] Fuster, D., Matas, J.-P., Marty, S., Popinet, S., Hoepffner, J., Cartellier, A. H., and Zaleski, S., 2013, "Instability regimes in the primary breakup region of planar coflowing sheets," Journal of Fluid Mechanics, **736**, pp. 150–176.

[9] Matas, J.-P., Delon, A., and Cartellier, A., 2018, "Shear instability of an axisymmetric air–water coaxial jet," Journal of Fluid Mechanics, **843**, pp. 575–600.

[10] Desjardins, O., Blanquart, G., Balarac, G., and Pitsch, H., 2008, "High order conservative finite difference scheme for variable density low Mach number turbulent flows," Journal of Computational Physics, **227**(15), pp. 7125–7159.

[11] Owkes, M. and Desjardins, O., 2014, "A computational framework for conservative, three-dimensional, unsplit, geometric transport with application to the volume-of-fluid (VOF) method," Journal of Computational Physics, **270**, pp. 587–612.

[12] Pilliod, J. E. and Puckett, E. G., 2004, "Second-order accurate volume-of-fluid algorithms for tracking material interfaces," Journal of Computational Physics, **199**(2), pp. 465–502.

[13] Meneveau, C., Lund, T. S., and Cabot, W. H., 1996, "A Lagrangian dynamic subgrid-scale model of turbulence," Journal of Fluid Mechanics, **319**, pp. 353–385.

[14] Wang, S. and Desjardins, O., 2018, "3D numerical study of large-scale two-phase flows with contact lines and application to drop detachment from a horizontal fiber," International Journal of Multiphase Flows, **101**, pp. 35–46.

[15] Popinet, S. and Zaleski, S., 1999, "A front-tracking algorithm for accurate representation of surface tension," International Journal for Numerical Methods in Fluids, **30**, pp. 775–793.

Table 1: Summary of simulation configurations: $Re_g = 21400$, $Re_l = 1200$, $M = 6.4$, $We = 39.1$.

Case	Gas Profile	Interface Boundary Condition
1	Analytical profile	Pinned at d_l
2	Analytical profile	Pinned at D_l
3	Partial nozzle modeled	Free with a static contact angle of 70°
4	Full nozzle modeled	Free with a static contact angle of 70°

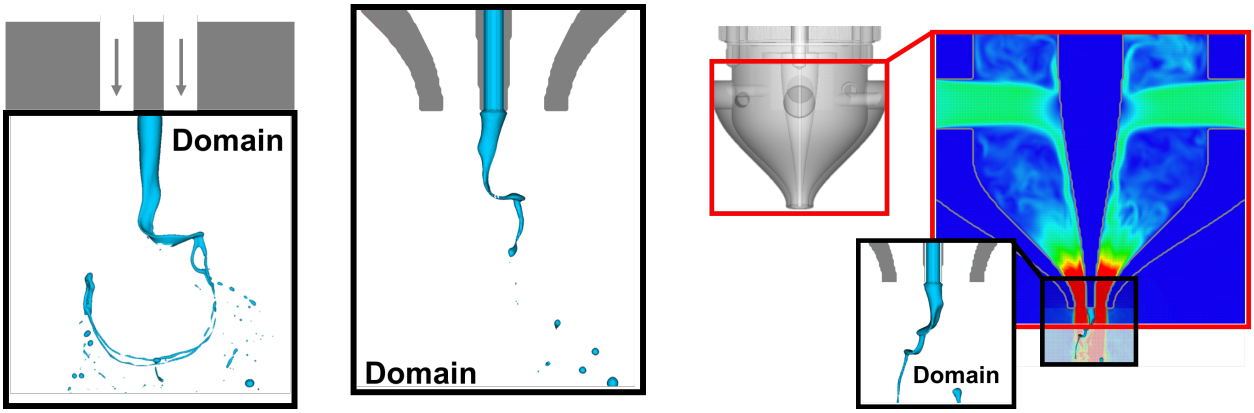

(a) Cases 1 and 2 (b) Case 3 (c) Case 4

Figure 1: Illustration of computational set up. a) Domain excludes the nozzle and utilizes an analytical profile to model the gas velocity. b) Part of the internal flow of nozzle is modeled. c) The full nozzle is modeled and used as inflow conditions to the atomization simulation.

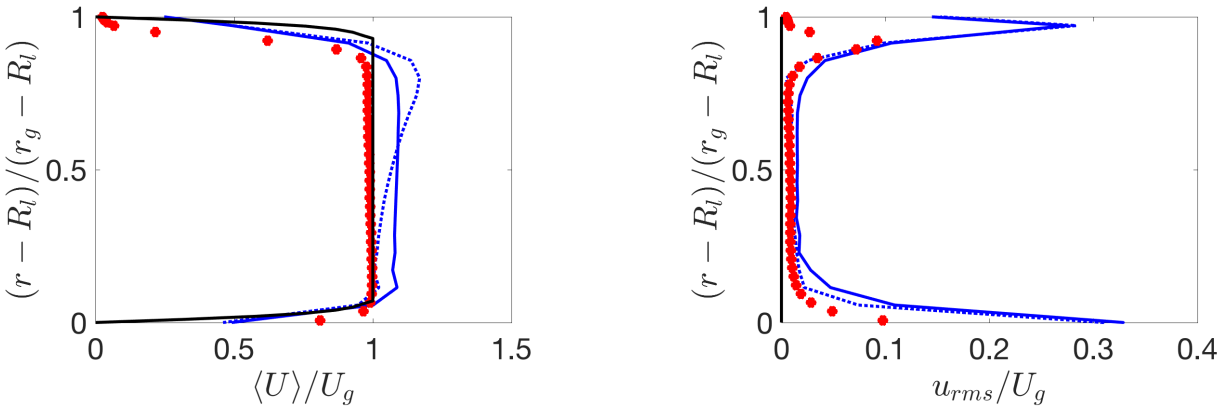

Figure 2: Comparison of velocity statistics. $R_l = 0.5D_l$ and $r_g = 0.5d_g$. Experiment (•), Analytical profile (——), Partial nozzle modeled (·····), Full nozzle modeled (——).

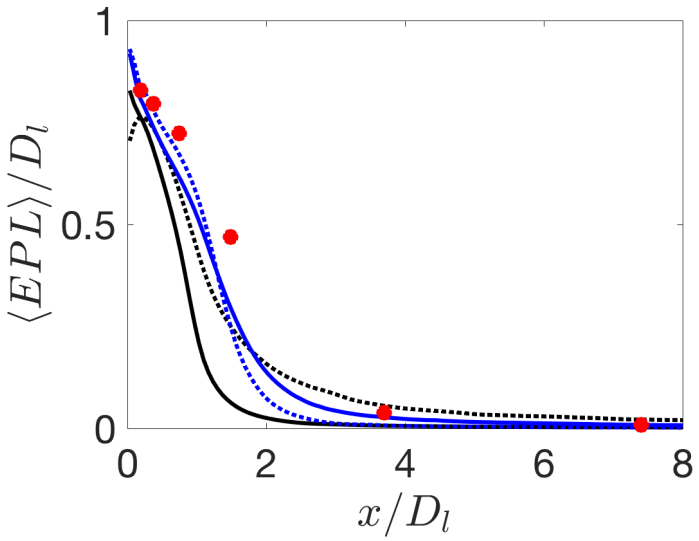

Figure 3: Centerline EPL profiles. Experiment (•), Case 1 (·····), Case 2 (——), Case 3 (·····), Case 4 (——).

Table 2: Comparison of time averaged liquid presence plots highlighting the asymmetry of case 3 and the axisymmetric behavior of case 4.

	x-y plane	x-z plane
Case 3: Partial nozzle modeled	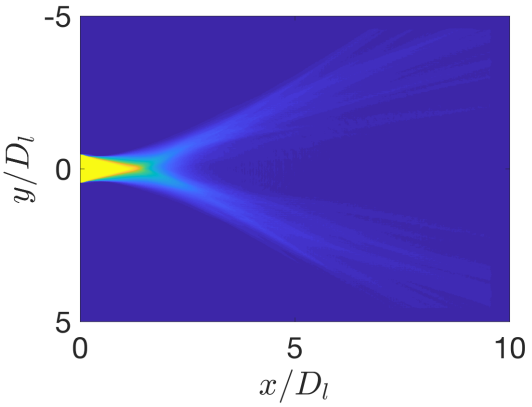	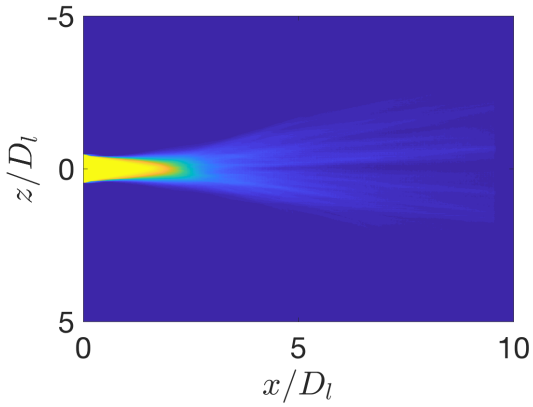
Case 4: Full nozzle modeled